Giant valley-Zeeman coupling in the surface layer of an intercalated transition-metal dichalcogenide

B. Edwards,[1] O. Dowinton,[2] A. E. Hall,[3] P. A. E. Murgatroyd,[1] S. Buchberger,[1,4] T. Antonelli,[1] G.-R. Siemann,[1] A. Rajan,[1] E. Abarca Morales,[1,4] A. Zivanovic,[1,4] C. Bigi,[1] R. V. Belosludov,[5] C. M. Polley,[6] D. Carbone,[6] D. A. Mayoh,[3] G. Balakrishnan,[3] M. S. Bahramy,[2,*] and P. D. C. King[1,†]

[1]*SUPA, School of Physics and Astronomy, University of St Andrews, St Andrews KY16 9SS, UK*
[2]*Department of Physics and Astronomy, University of Manchester, Oxford Road, Manchester M13 9PL, UK*
[3]*Department of Physics, University of Warwick, Coventry CV4 7AL, United Kingdom*
[4]*Max Planck Institute for Chemical Physics of Solids, Nöthnitzer Strasse 40, 01187 Dresden, Germany*
[5]*Institute for Materials Research, Tohoku University, Sendai 980-08577 Japan*
[6]*MAX IV Laboratory, Lund University, P. O. Box 118, 221 00 Lund, Sweden*

(Dated: November 25, 2022)

Spin-valley locking is ubiquitous to transition-metal dichalcogenides (TMDs) with local or global inversion asymmetry, in turn stabilising properties such as Ising superconductivity, and opening routes towards 'valleytronics'. The underlying valley spin splitting is set by spin-orbit coupling, but can be tuned via application of external magnetic fields or through proximity coupling. However, only modest changes have been realised to date. Here, we investigate the electronic structure of the V-intercalated TMD $V_{1/3}NbS_2$ using microscopic area spatially- and angle-resolved photoemission spectroscopy. Our measurements and corresponding density-functional theory calculations reveal that the bulk magnetic order induces a giant valley-selective Ising coupling exceeding 50 meV in the surface NbS_2 layer, equivalent to application of a ~ 250 T magnetic field. This is of comparable magnitude to the intrinsic spin-orbit splittings, and indicates how coupling of local magnetic moments to itinerant states of a TMD monolayer provides a powerful route to controlling their valley spin splittings.

NbS_2 is one of the most intriguing members of the transition-metal dichalcogenide (TMD) family. It is the only TMD to exhibit superconductivity which does not develop from a charge density wave state,[1,2] although it is thought to lie close to not only charge-ordering but also magnetic instabilities.[3] Intercalating transition metal ions (*e.g.* M=V, Cr, Co, Fe) into the van der Waals gap between neighbouring NbS_2 layers can lead to the development of long-range magnetic orders which host a variety of non-trivial spin textures.[4–8] Here, we consider the critical composition of $M_{1/3}NbS_2$ with M=V. The intercalated V atoms form an ordered structure, occupying distinct sites above and below each NbS_2 layer, V_1 and V_2, respectively (Fig. 1(a)), making the crystal non-centrosymmetric. Below a critical temperature, $T_N \approx 50$ K, the V spins order. Detailed neutron diffraction measurements[9] have revealed two co-existing components to the magnetism: an A-type antiferromagnetic order, confined within the ab-plane and consisting of ferromagnetic layers of V atoms coupled antiferromagnetically between layers; and a second component with moments aligned along the c-axis, and consisting of a 1-up 2-down longitudinal density wave-like modulation of the spins. Overall this forms a canted antiferromagnetic state (Fig. 1(b)), which is reported to lead to a net uncompensated ferromagnetic moment.[9,10]

As well as inducing magnetic order, the incorporation of nominally V^{3+} ions can be expected to lead to significant charge transfer into the NbS_2 layer as compared to pristine NbS_2.[11–13] Indeed, in a simple ionic picture, the V-intercalated compound can be viewed as an alternating stack of positively $[V_{1/3}]^+$ and negatively $[NbS_2]^-$ charged layers, with the NbS_2 layer thus electron doped relative to pristine NbS_2. Consistent with this, our density-functional theory (DFT) calculations of the charge density difference between $V_{1/3}NbS_2$ and NbS_2 (Fig. 1(a), see also Methods and Supplementary Fig. S1) indicate significant charge transfer from the V to the NbS_2 layers, with the V^{3+} cations acting as an ionic linkage between the otherwise weakly bonded NbS_2 layers.

Significant further modifications to the charge transfer can also be seen at the material surface. Charge transfer into a NbS_2 layer in the bulk from a V layer above can no longer occur at a NbS_2-terminated surface. The surface NbS_2 layer would thus be expected to become hole-doped as compared to its bulk counterpart. Conversely, a V-terminated surface would be expected to become electron-doped *cf.* the bulk. This simple picture is supported by our calculations of the surface electronic structure, shown in Supplementary Fig. S2, where the formation of new surface bands which result from compensating the polar surface charge can be viewed as a form of electronic reconstruction. This is similar to that discussed for the so-called 'polar catastrophe' origins of the two-dimensional electron gas at the $SrTiO_3/LaAlO_3$ interface[14] and for extreme self-doping at surfaces of *e.g.* some cuprates[15] and delafossite oxides.[16,17] We investigate this experimentally in Fig. 1(c-h).

Our samples were cleaved *in situ* before commencing photoemission measurements (see Methods). Given the covalent nature of the NbS_2 block, the NbS_2- and V-layer surface terminations discussed above and shown in Fig. 1(a) represent the natural cleavage planes of the crystal. Both terminations can be expected to be formed with equal probability, distributed randomly across the sample surface (with mixed and/or disordered terminations also possible[12]). We investigate this with spatially-resolved core level spectroscopy in Fig. 1(c-e). With the photon energies used here, our measurements are extremely surface sensitive, with a probing depth limited to the top few atomic layers.[18] The relative ratio of

integrated spectral weight of, for example, Nb 4p and V 3p core levels therefore provides a good measure of the topmost atomic species at the surface. As shown in Fig. 1(c), this ratio shows a strong spatial variation on a length scale of ca. 20-30 μm. We assign regions of higher (lower) intensity to NbS_2 (V) surface terminations, respectively.

Core level spectra extracted from representative regions of our spatial mapping data (see rectangles in Fig. 1(c)) are shown in Fig. 1(d,e). As well as their relative intensity variations, our measurements indicate a shift of the core level peaks to lower binding energy for the NbS_2-terminated surface with respect to the V-terminated surface. This is a direct experimental signature of the additional surface charge transfer discussed above, with hole doping at the NbS_2-terminated surface and electron doping at the V-terminated surface, as discussed further in Supplementary Note 1 and Supplementary Fig. S3. Interpretation of the S 2p core levels is more challenging due to the presence of well-defined surface core level components. Nonetheless, mapping of a pronounced component which develops at low binding energies for the NbS_2-terminated surface yields a spatial distribution that is in excellent agreement with that obtained by considering the Nb 4p:V 3p core level ratios in Fig. 1(c) (see Supplementary Fig. S4). Together, our core level measurements thus allow ready identification of distinct surface terminations, and point to a dominant electronic reconstruction as the route to compensate the corresponding polar surface charge.

The resulting surface charge transfer leads, in turn, to marked differences in the surface electronic structure. Fig. 1(g,h) shows the measured electronic structure integrated over the same spatial regions as for the core level spectra discussed above. For the V termination, we observe somewhat diffuse but dispersive features, which we attribute to NbS_2-derived bulk states, consistent with our calculations of such dispersive states in the bulk electronic structure of $V_{1/3}NbS_2$ shown in Supplementary Fig. S1. Additionally, we find rather non-dispersive spectral weight which likely results from the more localised V-derived states (see Supplementary Fig. S2).

The NbS_2 termination, on the other hand, hosts a much richer electronic structure. In particular, we find several sharp dispersive states in the vicinity of the Fermi level. These appear to be hole-doped analogues of the dispersive states observed for the V termination. From photon energy-dependent measurements (see Supplementary Figs. S5 and S6) we find the new states arising on the NbS_2 termination are strictly two-dimensional. Integrating the spectral weight over these dispersive states (dashed region shown in Fig. 1(g,h)), we find a spatial intensity distribution (Fig. 1(f)) which closely resembles that derived from the core level spectra (Fig. 1(c)). We thus attribute these new dispersive states as surface states of the NbS_2-terminated surface of $V_{1/3}NbS_2$.

We show in Fig. 2(a,b) higher-resolution measurements of the low-energy electronic structure of the NbS_2-terminated surface, measured below the bulk magnetic ordering temperature. The surface bands are split-off from the underlying bulk $V_{1/3}NbS_2$ bands due to the self-doping at this polar surface, becoming located in projected band gaps of the bulk electronic structure (see also Supplementary Fig. S2). They are thus well localised at the surface, and, in a simple picture, can be viewed as deriving from a monolayer-like surface NbS_2 layer. For the broken inversion symmetry inherent to such a monolayer, spin-orbit coupling lifts the spin degeneracy, leading to a locking of quasiparticle spin to a valley pseudospin as is evident in Fig. 2(d), *i.e.* a spin-valley locking results.[19–24]

Signatures of the electronic structure that would be expected for such a NbS_2 monolayer (Fig. 2(c,d)) can be identified in our experimental measurements. In particular, we observe a large hexagonal pocket around the Brillouin zone centre (labelled β in Fig. 2(a,c)) and two split-off states (which we denote $\alpha_{1,2}$) which disperse upwards towards the K point of the NbS_2 Brillouin zone, forming a pair of hole-like barrels centered at this zone corner point. The Fermi pockets observed experimentally (Fig. 2(b)) are qualitatively similar to those in the calculations of monolayer NbS_2 (Fig. 2(d)), although are significantly smaller. This size mismatch can largely be understood as a consequence of the charge transfer discussed above: while the $[NbS_2]^-$ layer in bulk $V_{1/3}NbS_2$ is formally expected to have a d^2 charge count, an additional nominal hole doping of 0.5 holes/formula unit at the NbS_2-terminated surface should render the surface layer in a $d^{1.5}$ configuration, electron-doped by 0.5 electrons/formula unit as compared to a pristine NbS_2 monolayer. Indeed, from a Luttinger analysis of the experimentally-measured Fermi surfaces, we find an electron count of the NbS_2 surface layer of 1.48 ± 0.02, in agreement within experimental error of that predicted from our simple charge transfer arguments.

There are, however, a number of important differences in the measured electronic structure with respect to a simple doped NbS_2 monolayer. The first is an evident doubling of all of the states, with a replica of the large hexagonal pocket also found centered at each Brillouin zone corner (β^{bf}), and additional smaller pockets found at the Brillouin zone centre ($\alpha^{\mathrm{bf}}_{1,2}$). This is a signature of a new periodicity induced by the sub-surface V atoms. As shown in Fig. 2(e), a V atom is located directly below one in every 3 surface Nb atoms, leading to a new periodic potential with a $\sqrt{3}\times\sqrt{3}R30^\circ$ periodicity as compared to a pristine NbS_2 monolayer.[4,9] This is evident in our low-energy electron diffraction measurements in Fig. 2(f), generating a reduced and rotated Brillouin zone shown by the dashed line in Fig. 2(b).

The electronic states from the larger parent NbS_2 zone will become backfolded about the new Brillouin zone boundary, leading to the additional pockets discussed above. The opening of hybridisation gaps can be expected at the new Brillouin zone boundary $\overline{\mathrm{M}}$ points, and these are evident in our measured dispersions in Fig. 2(a) (see also Supplementary Fig. S8). Even considering this backfolding, however, there remains an intriguing discrepancy with the expected electronic structure for a NbS_2 monolayer. Specifically, the $\alpha_{1,2}$ bands along the Γ-K line exhibit significant splittings, while along Γ-K', the band splitting between these states appears to be absent (see also additional data in Supplementary Fig. S9). This leads to a Fermi pocket splitting that is strongly modulated with the valley index (Fig. 2(b)).

From spatial mapping data shown in Fig. 3(a-c), we find that there are distinct regions for which the splitting of the

Nb-derived conduction band ($\alpha_{1,2}$) appears on the positive (Fig. 3(b), orange colouring in the inset of Fig. 3(a)) or negative (Fig. 3(c), purple colouring in Fig. 3(a)) side of our measured momentum. This suggests that the momentum-dependent modulation of the band splittings observed here may be of magnetic origin, with the signs of the splitting reversed for different magnetic domains of the bulk antiferromagnetic order. To confirm this interpretation, we show in Fig. 3(d-g) measurements of the evolution of the band splitting within a single domain as a function of temperature. At low temperature (Fig. 3(g)), the clear asymmetry in splitting of the $\alpha_{1,2}$ bands for positive and negative momentum is evident in Fermi level momentum-distribution curves (MDCs) shown in Fig. 3(e,f): a clear two-peak structure is observed near the K point, but a single sharp (albeit slightly asymmetric) peak is observed near the K' point. In contrast, the high-temperature Fermi level MDCs extracted near K and K' are mirror-symmetric copies of each other. The observed peaks are broad and rather flat-topped, indicating the presence of two components and hence a remnant band splitting, but one which is the same for both positive and negative momenta (see also Supplementary Fig. S7).

The MDC peak splitting evolves smoothly between the low- and high-temperature limits up to temperatures of $\sim$50 K, and remains rather static above this. This is confirmed from the Fermi level momentum splitting, Δk_{F}, extracted from fits to our MDCs (Fig. 3(h)): the high-temperature band splitting is found to be identical within experimental error for the positive and negative momentum sides, while it diverges below a critical temperature of $\sim$ 53 K, growing on the positive momentum side and collapsing to near zero on the negative momentum side. Magnetic susceptibility data from our samples (Fig. 3(i)) indicates that the onset of the change in band splitting occurs precisely at the magnetic transition temperature.

Our temperature-dependent measurements thus indicate that the unusual momentum-dependent band splittings observed at low-temperature (Fig. 2(a,b)) result from exchange coupling of the itinerant NbS_2-derived surface states to local magnetic moments on the underlying V sites. To confirm this, we extract the corresponding energetic shifts of the NbS_2 surface band from our temperature-dependent ARPES measurements (see Supplementary Figs. S10 and S11). The resulting temperature-dependent changes in band position well reproduce the measured magnetic susceptibility, indicating that they reflect an order parameter of the magnetisation, and thus can be assigned as an exchange splitting.

To explore the origin of this exchange coupling further, we show in Fig. 4(a) calculations of the real-space projected spin density isosurfaces for bulk $V_{1/3}NbS_2$, performed for a simple antiferromagnetic configuration. We find a spatially alternating spin density, predominantly localised around the V ions but with partial fragmentation within the intermediate NbS_2 layers. The shape of the spin density distribution around the Nb sites is strikingly similar to that of a d_{z^2} orbital, which, as shown in Supplementary Fig. S1, is the primary contributor to the only band crossing the Fermi level in bulk $V_{1/3}NbS_2$. Moreover, they carry a sign opposite to that of their adjacent V sites, together directly indicating an exchange interaction between V mangetisation and the spins of the itinerant Nb electrons.

To further confirm this picture, we have performed bulk-sensitive resonant photoemission measurements at the V $L_{2,3}$ edge, allowing us to selectively enhance spectral weight derived from the V d-orbitals. Our measurements (see Supplementary Fig. S12) indicate that the V states contribute a well-defined peak in the density of states at a binding energy of $\sim$ 1 eV, with negligible weight persisting to the Fermi level. This is unlike the case for the Cr- and Co-based sister compounds,[13,25,26] where more significant band hybridisation in the vicinity of the Fermi level has been proposed (see also Supplementary Fig. S13 where we compare surface termination-dependent ARPES data of $V_{1/3}NbS_2$ and $Cr_{1/3}NbS_2$). Instead, in $V_{1/3}NbS_2$, our measurements demonstrate that there is minimal band hybridisation between the V and Nb-derived states at the Fermi level.

While further studies are required to definitively identify the magnetic exchange pathways, these findings, together with the large V-V real-space distance, are suggestive of a carrier-mediated Ruderman-Kittel-Kasuya-Yosida (RKKY)-like exchange interaction[27,28] underpinning the magnetic ordering of $V_{1/3}NbS_2$. Crucially, and irrespective of the precise heirarchy of exchange couplings here, our observations of pronounced temperature-dependent shifts in the surface band structure can unambiguously be identified as the result of an induced moment in the Nb-derived itinerant states. To understand the critical role of this coupling on the electronic structure, we model the NbS_2 surface layer as a NbS_2 monolayer with time-reversal symmetry breaking from proximity coupling to a magnetic layer beneath. Specifically, we consider hopping terms for the NbS_2 monolayer, and add the coupling to V as a splitting on the spin sub-space, to construct a tight binding Hamiltonian for the Nb $d_{xy}, d_{x^2-y^2}, d_{z^2}$, and S p_x, p_y, p_z orbitals with the form:

$$\mathcal{H} = \mathcal{H}_0 + \mathcal{H}_{\mathrm{ex}}, \tag{1}$$

where $\mathcal{H}_0$ is the Hamiltonian of an unperturbed NbS_2 monolayer, and $\mathcal{H}_{\mathrm{ex}}$ describes the spin splitting that results from the magnetic exchange:

$$\mathcal{H}_{\mathrm{ex}} = \sum_i J_i \boldsymbol{S_i} \cdot \boldsymbol{S}_{\mathrm{V}}, \tag{2}$$

where J_i is the effective exchange coupling between the spin operator $\boldsymbol{S_i}$ on the NbS_2 site i, and the spin operator $\boldsymbol{S}_{\mathrm{V}}$ on the adjacent V site. This can be decomposed into two contributions, $\mathcal{H}_{\mathrm{ex}}^{\parallel}$ and $\mathcal{H}_{\mathrm{ex}}^{\perp}$, arising from two distinct coupling processes $J_{\parallel}$ and $J_{\perp}$ between the V d orbitals and the in-plane $\{d_{xy}, d_{x^2-y^2}\}$ and out-of-plane d_{z^2} NbS_2 orbitals, as shown in Fig. 4(b,c), respectively.

Considering an exchange field directed along [001] (see Supplementary Figs. S14 and S15 for a discussion of additional field configurations and a comparison of first-principles and experimentally-derived exchange parameters), we examine the effect each coupling mechanism has on the spin splitting as a perturbation from the case with only spin-orbit coupling (SOC) included. From the orbital projections of the

SOC-only calculation shown in Fig. 2(c), one can anticipate that at Γ the exchange splitting will be dominated by the $\mathcal{H}_{\text{ex}}^{\perp}$ term, and at K/K' dominated by $\mathcal{H}_{\text{ex}}^{\parallel}$. Consistent with this, we find in Fig. 4(d,e) that the $\mathcal{H}_{\text{ex}}^{\parallel}$ term leads to significant modifications in the electronic structure close to the K and K' points as compared to the calculations with only SOC, while the electronic structure is almost unchanged close to Γ. In contrast, for the $\mathcal{H}_{\text{ex}}^{\perp}$ term, exchange splittings are observed close to the Brillouin zone centre, while the valley spin splitting around the K and K' points is little changed from that shown in Fig. 2.

We include both of these exchange contributions in our model, as well as the band-folding arising from the subsurface V-induced superlattice potential, which is visible in our ARPES measurements, as discussed above, but with reduced spectral intensity. Through this, we find a Fermi surface that is in excellent agreement with the one we observe experimentally (Fig. 4(f)). This includes both the valley-dependent spin splitting at the K and K' points, and also the azimuthal angle-dependent splittings of the $\alpha_{1,2}^{\text{bf}}$ Fermi pockets backfolded to the Brillouin zone centre.

From the Fermi surface shown in Fig. 4(f), it is clear that at and below the Fermi level, the changes in electronic structure we observe are dominated by exchange couplings between V d and the NbS_2 planar orbitals (Fig. 4(b,d)), with the exchange and SOC-induced spin splittings acting to enhance each other at the K point, while opposing each other at K' (Fig. 4(d)). This is because the exchange interaction is valley independent, while the SOC splitting is of equal magnitude but opposite sign for each valley. Therefore, the total valley splitting here can be captured by the simple expression:

$$\Delta = J_{\parallel} + \tau\Delta_{\text{SO}}, \tag{3}$$

where $\tau = \pm 1$ is the valley index.

We thus attribute the change in surface electronic structure observed here upon cooling through the magnetic ordering temperature as due to a giant valley-selective Ising coupling (a so-called 'valley-Zeeman coupling'[29–32]). From fits of the band splittings from our measured ARPES dispersions (see Supplementary Fig. S11), we estimate a total exchange splitting, $\Delta_{\text{ex}} = 52 \pm 7$ meV. This is of comparable magnitude to the full intrinsic spin-orbit splittings observed in the normal state, which we estimate as $\Delta_{\text{SO}} = 59 \pm 4$ meV. As a result, we find a near spin degeneracy is recovered for one valley at low temperature, while a total spin splitting in excess of 110 meV is obtained for the other. Typical g-factors for TMDs lead to a valley-Zeeman splitting in an externally-applied field of only ~ 0.2 meV/T.[29] The splittings realised here would therefore require application of a magnetic field exceeding 250 T. Even if it were possible to apply such a large external field, that in itself would act to decouple the electron spin from its orbital degree of freedom, while the giant orbitally-driven Ising exchange coupling observed here remains accessible through the magnetic proximity effect.

Our measurements of $V_{1/3}NbS_2$ thus indicate how exchange coupling between local moments and itinerant states provide a critical route to enhanced control over valley spin splittings in TMDs. These can be readily tuned by modest changes in temperature and provide substantially larger responses compared to other proximity-coupling schemes utililsed to date.[33–35] Key to this giant effect is the strong coupling between the magnetic and itinerant layers here (Fig. 4a). Excitingly, there is a large and rich family of intercalated TMDs, hosting distinct TMD layers, magnetic orders and critical temperatures. Furthermore, there is evidence of more substantial hybridisation between the intercalated metal and TMD states for some such compounds than was observed here for $V_{1/3}NbS_2$.[4,25,26] This raises the tantalising prospect to gain additional control over spin splittings in the TMD layer, and to couple the effects observed here with other collective states.

Acknowledgements: We thank M. Leandersson and T. Balasubramanian for useful discussions. We gratefully acknowledge support from the Leverhulme Trust (Grant No. RL-2016-006 [P.D.C.K., B.E., T.A., A.R., C.B.]), the European Research Council (through the QUESTDO project, 714193 [P.D.C.K., G.R.S.]), the Engineering and Physical Sciences Research Council (Grant Nos. EP/T02108X/1 [P.D.C.K., P.A.E.M.] and EP/N032128/1 [D.A.M., G.B.]), and the Center for Computational Materials Science at the Institute for Materials Research for allocations on the MASAMUNE-IMR supercomputer system (Project No. 202112-SCKXX-0510 [R.B.V., M.S.B.]). S.B., E.A.M. and A.Z. gratefully acknowledge studentship support from the International Max-Planck Research School for Chemistry and Physics of Quantum Materials. We gratefully acknowledge MAX IV Laboratory for time on the Bloch beamline under Proposal Nos. 20200227, 20210091, and 20210763. Research conducted at MAX IV, a Swedish national user facility, is supported by the Swedish Research council under contract 2018-07152, the Swedish Governmental Agency for Innovation Systems under contract 2018-04969, and Formas under contract 2019-02496. The research leading to this result has been supported by the project CALIPSOplus under the Grant Agreement 730872 from the EU Framework Programme for Research and Innovation HORIZON 2020. For the purpose of open access, the authors have applied a Creative Commons Attribution (CC BY) licence to any Author Accepted Manuscript version arising.

Author contributions The ARPES data was measured by BE, PAEM, SB, TA, GS, AR, EAM, AZ, CB, and PDCK, and analysed by BE. OD, RVB, and MSB performed the DFT and tight binding calculations. AEH, DM, and GB grew and characterised the samples. CMP and DC maintained the Bloch beamline and provided experimental support. BE, OD, MSB and PDCK wrote the manuscript with input and contributions from all authors.

Competing interests The authors declare no competing interests.

Figure captions

FIG. 1. **Surface termination-dependent electronic structure of $V_{1/3}NbS_2$.** (a) Crystal structure of $V_{1/3}NbS_2$, displaying the bulk and distinct surface termination-dependent charge transfers as compared to pristine NbS_2, calculated using DFT. (b) Bulk magnetic structure from Ref.,[9] displaying the relative orientation of local magnetic moments on the V sites in two side-by-side magnetic unit cells. (c) X-ray photoelectron spectroscopy (XPS) spatial map displaying the ratio of the integrated spectral weight of Nb $4p$ to V $3p$ core levels. High (yellow) and low (blue) intensity regions correspond to the NbS_2 and V surface terminations, respectively. (d,e) Core level spectra for the NbS_2 (brown) and V (blue) surface terminations (T = 19 K, $h\nu$ = 200 eV, LH polarisation), extracted from the regions indicated in (c). Shaded red and green regions indicate the energies over which the V $3p$ and Nb $4p$ core levels were integrated to produce the spatial map in (c). (f) Spatial map derived by integrating microscopic area spatially- and angle-resolved photoemission spectroscopy (μ-ARPES) data over the region of interest shown by the dashed lines in (g) and (h), corresponding to a NbS_2 surface state. (g,h) Corresponding dispersions of the (g) V and (h) NbS_2 surface terminations (T = 19 K, $h\nu$ = 100 eV, LH polarisation), extracted from the regions indicated in (f).

FIG. 2. **Low-energy electronic structure of the NbS_2-terminated surface**. (a) ARPES dispersion along K'-Γ-K measured at T = 20 K ($h\nu$ = 70 eV, LH polarisation), and (b) corresponding Fermi surface ($h\nu$ = 79 eV, LV polarisation). A three-fold rotational symmetrisation has been applied for clarity of presentation; the same band structure features are, however, visible in the non-transformed data (see Supplementary Fig. S7). (c,d) DFT calculations showing the (c) low-energy electronic structure and (d) Fermi surface expected for a pristine monolayer of NbS_2, with projected orbital and spin character, respectively. (e) Top-down view of the NbS_2 surface termination of $V_{1/3}NbS_2$, with real space unit cells of a NbS_2 layer and $V_{1/3}NbS_2$ indicated. (f) Low-energy electron diffraction measurements indicate how the sub-surface V atoms give rise to a $\sqrt{3}\times\sqrt{3}R30^\circ$ superstructure, which leads to the reduced Brillouin zone shown by the dashed lines in (a) and (b). Corresponding band folding is evident about these Brillouin zone boundaries, while additional chemical potential shifts and momentum-dependent band splittings are observed in the experimental data *cf.* the calculations of the pristine monolayer.

FIG. 3. **Valley-dependent band splitting from magnetic exchange.** (a) Spatial map displaying the integrated spectral weight of the NbS_2-terminated surface state as performed in Fig. 1(e) (T = 21 K, $h\nu$ = 79 eV, LV polarisation) but from a different cleave of the sample. The inset shows the observation of different domains where the splitting of the α band is found at positive (orange regions) or negative (purple regions) sides of our measured momentum. To generate this inset, MDCs at the Fermi level were fit from the underlying dispersions, with the 'Δ valley splitting' determined as the difference of the extracted Δk_F of the α_1 and α_2 bands between the two momentum sides. (b,c) Measured dispersions extracted from the regions marked in the inset of (a). Double (single) arrows indicate the split (merged) bands. (d-g) Temperature-dependent measurements along the K'-Γ-K direction ($h\nu$ = 70 eV, LH polarisation) from within a single domain. The dispersions measured at (d) 70 K and (g) 21 K show a marked change in the band splittings, which are also evident in temperature-dependent MDCs at the Fermi level extracted along the dashed lines shown in (d) and (g) across the α_1 and α_2 bands near (e) K' and (f) K. (h) Δk_F of the α_1 and α_2 bands in the positive (near K) and negative (near K') momentum directions extracted from fits to these MDCs. These indicate a band splitting which is constant for both directions at high temperature, but which diverge below the magnetic ordering temperature, as evident by comparison to the field-cooled DC magnetic susceptibility shown in (i), measured in an applied field of H=330 Oe ($H \perp$ c). The functional form of the susceptibility data here is a result of a net uncompensated ferromagnetic moment for the bulk magnetic structure of $V_{1/3}NbS_2$.[9] Error bars in (h) reflect an approximate estimate of the uncertainty in extracting the underlying peak positions from the experimental measurements, incorporating statistical errors in peak fitting, systematic errors, and experimental resolution.

FIG. 4. **Orbital-selective magnetic exchange coupling.** (a) Calculated spin density distribution at and near the NbS_2-terminated surface of $V_{1/3}NbS_2$ at a fixed value of 0.001 eÅ^{-3}. The red and cyan colours correspond to the spin-up and spin-down states, respectively. (b,c) Schematic models demonstrating magnetic Ising coupling between the topmost subsurface V $3d$ orbitals with (b) their adjacent in-plane S $\{p_x, p_y\}$ and Nb $\{d_{xy}, d_{x^2-y^2}\}$ orbitals and (c) the out-of-plane S p_z and Nb d_{z^2} orbitals within the topmost NbS_2 layer, indicated by a grey rectangle in (a). (d,e) The spin-projected band structures resulting from the exchange pathways illustrated in (b) and (c), respectively. (f) The calculated Fermi surface combining the contributions in (b) and (c), along with band folding from the structural superlattice potential. The resulting calculated Fermi surface shows a strong valley-dependent modulation of the spin splitting of the electronic states, in good agreement with the ARPES data shown beneath.

* m.saeed.bahramy@manchester.ac.uk
† pdk6@st-andrews.ac.uk

[1] Guillamón, I. *et al.* Superconducting Density of States and Vortex Cores of 2H-NbS_2. *Phys. Rev. Lett.* **101**, 166407 (2008).
[2] Heil, C. *et al.* Origin of Superconductivity and Latent Charge Density Wave in NbS_2. *Phys. Rev. Lett.* **119**, 087003 (2017).
[3] van Loon, E. G. C. P., Rösner, M., Schönhoff, G., Katsnelson, M. I. & Wehling, T. O. Competing Coulomb and electron–phonon interactions in NbS_2. *npj Quantum Mater.* **3**, 32 (2018).
[4] Parkin, S. S. P. & Friend, R. H. 3d transition-metal intercalates of the niobium and tantalum dichalcogenides. II. Transport properties. *Philos. mag. B* **41**, 95–112 (1980).
[5] Kousaka, Y. *et al.* Chiral helimagnetism in $T_{1/3}NbS_2$ (T=Cr and Mn). *Nucl. Instrum. Methods Phys. Res. A* **600**, 250–253 (2009).

[6] Togawa, Y. *et al.* Chiral Magnetic Soliton Lattice on a Chiral Helimagnet. *Phys. Rev. Lett.* **108**, 107202 (2012).

[7] Nair, N. L. *et al.* Electrical switching in a magnetically intercalated transition metal dichalcogenide. *Nat. Mater.* **19**, 153–157 (2020).

[8] Little, A. *et al.* Three-state nematicity in the triangular lattice antiferromagnet $Fe_{1/3}NbS_2$. *Nat. Mater.* **19**, 1062–1067 (2020).

[9] Hall, A. E. *et al.* Magnetic structure investigation of the intercalated transition metal dichalcogenide $V_{1/3}NbS_2$. *Phys. Rev. B* **103**, 174431 (2021).

[10] Lu, K. *et al.* Canted antiferromagnetic order in the monoaxial chiral magnets $V_{1/3}TaS_2$ and $V_{1/3}NbS_2$. *Phys. Rev. Mater.* **4**, 054416 (2020).

[11] Battaglia, C. *et al.* Non-uniform doping across the Fermi surface of NbS_2 intercalates. *Eur. Phys. J. B* **57**, 385–390 (2007).

[12] Sirica, N. *et al.* Electronic structure of the chiral helimagnet and 3d-intercalated transition metal dichalcogenide $Cr_{1/3}NbS_2$. *Phys. Rev. B* **94**, 075141 (2016).

[13] Tanaka, H. *et al.* Large anomalous hall effect induced by weak ferromagnetism in the noncentrosymmetric antiferromagnet $CoNb_3S_6$. *Phys. Rev. B* **105**, L121102 (2022).

[14] Nakagawa, N., Hwang, H. Y. & Muller, D. A. Why some interfaces cannot be sharp. *Nat. Mater.* **5**, 204–209 (2006).

[15] Hossain, M. A. *et al.* In situ doping control of the surface of high-temperature superconductors. *Nat. Phys.* **4**, 527–531 (2008).

[16] Sunko, V. *et al.* Maximal Rashba-like spin splitting via kinetic-energy-coupled inversion-symmetry breaking. *Nature* **549**, 492–496 (2017).

[17] Mazzola, F. *et al.* Itinerant ferromagnetism of the Pd-terminated polar surface of $PdCoO_2$. *PNAS* **115**, 12956–12960 (2018).

[18] Seah, M. P. & Dench, W. A. Quantitative electron spectroscopy of surfaces: A standard data base for electron inelastic mean free paths in solids. *Surf. Interface Anal.* **1**, 2–11 (1979).

[19] Xiao, D., Liu, G.-B., Feng, W., Xu, X. & Yao, W. Coupled Spin and Valley Physics in Monolayers of MoS_2 and Other Group-VI Dichalcogenides. *Phys. Rev. Lett.* **108**, 196802 (2012).

[20] Mak, K. F., He, K., Shan, J. & Heinz, T. F. Control of valley polarization in monolayer MoS_2 by optical helicity. *Nat. Nanotechnol.* **7**, 494–498 (2012).

[21] Zeng, H., Dai, J., Yao, W., Xiao, D. & Cui, X. Valley polarization in MoS_2 monolayers by optical pumping. *Nat. Nanotechnol.* **7**, 490–493 (2012).

[22] Riley, J. M. *et al.* Direct observation of spin-polarized bulk bands in an inversion-symmetric semiconductor. *Nat. Phys.* **10**, 835–839 (2014).

[23] Bawden, L. *et al.* Spin–valley locking in the normal state of a transition-metal dichalcogenide superconductor. *Nat. Commun.* **7**, 11711 (2016).

[24] Xu, X., Yao, W., Xiao, D. & Heinz, T. F. Spin and pseudospins in layered transition metal dichalcogenides. *Nat. Phys.* **10**, 343–350 (2014).

[25] Sirica, N. *et al.* The nature of ferromagnetism in the chiral helimagnet $Cr_{1/3}NbS_2$. *Commun. Phys.* **3**, 65 (2020).

[26] Popčević, P. *et al.* Role of intercalated cobalt in the electronic structure of $Co_{1/3}NbS_2$. *Phys. Rev. B* **105**, 155114 (2022).

[27] Yosida, K. Magnetic properties of Cu-Mn alloys. *Phys. Rev.* **106**, 893–898 (1957).

[28] Geldenhuys, J. & Wiid, D. H. RKKY interaction and conduction electron polarisation. *J. Phys. F: Met. Phys.* **8**, 2021–2033 (1978).

[29] Srivastava, A. *et al.* Valley Zeeman effect in elementary optical excitations of monolayer WSe_2. *Nat. Phys.* **11**, 141–147 (2015).

[30] Aivazian, G. *et al.* Magnetic control of valley pseudospin in monolayer WSe_2. *Nat. Phys.* **11**, 148–152 (2015).

[31] Li, Y. *et al.* Valley Splitting and Polarization by the Zeeman Effect in Monolayer $MoSe_2$. *Phys. Rev. Lett.* **113**, 266804 (2014).

[32] MacNeill, D. *et al.* Breaking of Valley Degeneracy by Magnetic Field in Monolayer $MoSe_2$. *Phys. Rev. Lett.* **114**, 037401 (2015).

[33] Zhong, D. *et al.* Van der Waals engineering of ferromagnetic semiconductor heterostructures for spin and valleytronics. *Sci. Adv.* **3**, e1603113 (2017).

[34] Zhong, D. *et al.* Layer-resolved magnetic proximity effect in van der Waals heterostructures. *Nat. Nanotechnol.* **15**, 187–191 (2020).

[35] Norden, T. *et al.* Giant valley splitting in monolayer WS_2 by magnetic proximity effect. *Nat. Commun.* **10**, 4163 (2019).

Methods

Sample preparation and characterisation: Single crystal samples of $V_{1/3}NbS_2$ were grown using the chemical vapour transport method with iodine as a transport agent. An evacuated quartz ampoule was slowly heated until a temperature gradient of 950°C to 850°C was applied across it, with polycrystalline $V_{1/3}NbS_2$ situated in the 950°C region of the ampoule acting as a seed for the growth. After 500 hours, the ampoule was slowly cooled. Temperature-dependent dc magnetisation measurements were performed on single crystal samples mounted in general electric varnish on a non-magnetic straw in a Quantum Design Magnetic Property Measurement System (MPMS). The single crystals were aligned so that the applied field was perpendicular to the c axis of the crystals. The crystal was measured over a temperature range of 5 to 80 K in a field of 330 Oe.

μ-ARPES: Spatially-resolved ARPES and XPS measurements were performed at the Bloch beamline of MAX IV Laboratory, using linearly-polarised light with photon energies between 25 and 200 eV, and with a probing spot size of 10×15 μm^2. The samples were mounted on a conventional 6-axis manipulator which allowed cooling to 20 K. The samples were cleaved *in situ* at base temperature, and measured using a Scienta DA30 electron analyser.

Calculations: Electronic structure calculations were performed within DFT using the Perdew–Burke–Ernzerhof exchange-correlation functional,[1] as implemented in the VASP programme.[2,3] Relativistic effects, including spin-orbit coupling, were fully included. For the bulk calculations, we considered a $\sqrt{3} \times \sqrt{3} \times 1$ supercell containing six formula units of NbS_2 and two intercalated V atoms antiferromagnetically ordered along the $[001]$ axis, as shown in Fig. 4(a). The corresponding Brillouin zone was sampled by a $15 \times 15 \times 10$ k-mesh. An additional onsite Hubbard term with an effective U value of 2 eV was added to V $3d$ orbitals to reproduce the experimentally observed alignment of V bands with respect to the valence continuum of NbS_2.

To compute the excess and depletion charge distribution due to the V intercalation, we first calculated the charge density for a 5-layer slab of $V_{1/3}NbS_2$ stacked along the crystalline c-axis with a vacuum thickness of 15 Å and two different terminations, shown in Fig 1(a). The BZ sampling was done using a $20 \times 20 \times 1$ k-mesh. We next calculated the charge densities from the NbS_2 and V centres individually by removing V and NbS_2 layers in the same slab, respectively. Finally, we subtracted these individual contributions from the $V_{1/3}NbS_2$ charge density, treating the remaining as excess (wherever it was positive) or depletion (wherever it was negative) charge density.

To model valley-Zeeman coupling, we carried out a separate DFT calculation for a monolayer of NbS_2 within the same level of theory as that of the slab calculations. From this, we constructed a 22-band tight binding model using Wannier functions[4] with Nb d and S p orbitals as the projection centres. This model was then reduced to a 4-band model in the basis of $\{d_{xy}, d_{x^2-y^2}\}$ and d_{z^2}. An Ising-like exchange coupling term $\mathcal{H}_{\text{ex}}$ was further included to account for the magnetic interactions, as discussed further in the main text. The exchange coupling constants are first deduced from the nearest neighbour Nb-V hopping parameters interpolated from a first-principles calculation performed on bulk $V_{1/3}NbS_2$ using maximally localised Wannier functions. They are then slightly modified empirically to best match the experimental data. This leads to only small quantitative changes in the electronic structure, as shown in Supplementary Fig. S15. The best agreement with the experiment is for $J_{\parallel} = 50$ meV and $J_{\perp} = 60$ meV.

Data availability The research data supporting this publication can be accessed at https://doi.org/10.17630/fb5496ed-6eae-49fa-9214-cd3507265f2b.[5]

Code availability The codes used in this study are available either publicly (Wannier90; http://www.wannier.org) or through subscription (VASP; https://www.vasp.at). For a detailed description of input parameters used for each code, refer to Calculations. Further inquires should be addressed to the corresponding authors.

* m.saeed.bahramy@manchester.ac.uk
† pdk6@st-andrews.ac.uk

[1] Perdew, J. P., Burke, K. & Ernzerhof, M. Generalized gradient approximation made simple. *Phys. Rev. Lett.* **77**, 3865–3868 (1996).
[2] Kresse, G. & Furthmüller, J. Efficient iterative schemes for ab initio total-energy calculations using a plane-wave basis set. *Phys. Rev. B* **54**, 11169–11186 (1996).
[3] Kresse, G. & Joubert, D. From ultrasoft pseudopotentials to the projector augmented-wave method. *Phys. Rev. B* **59**, 1758–1775 (1999).
[4] Mostofi, A. A. *et al.* wannier90: A tool for obtaining maximally-localised Wannier functions. *Comput. Phys. Commun.* **178**, 685–699 (2008).
[5] Edwards, B. *et al.* Giant valley-Zeeman coupling in the surface layer of an intercalated transition-metal dichalcogenide (dataset). *Dataset. University of St Andrews Research Portal.*, https://doi.org/10.17630/fb5496ed-6eae-49fa-9214-cd3507265f2b

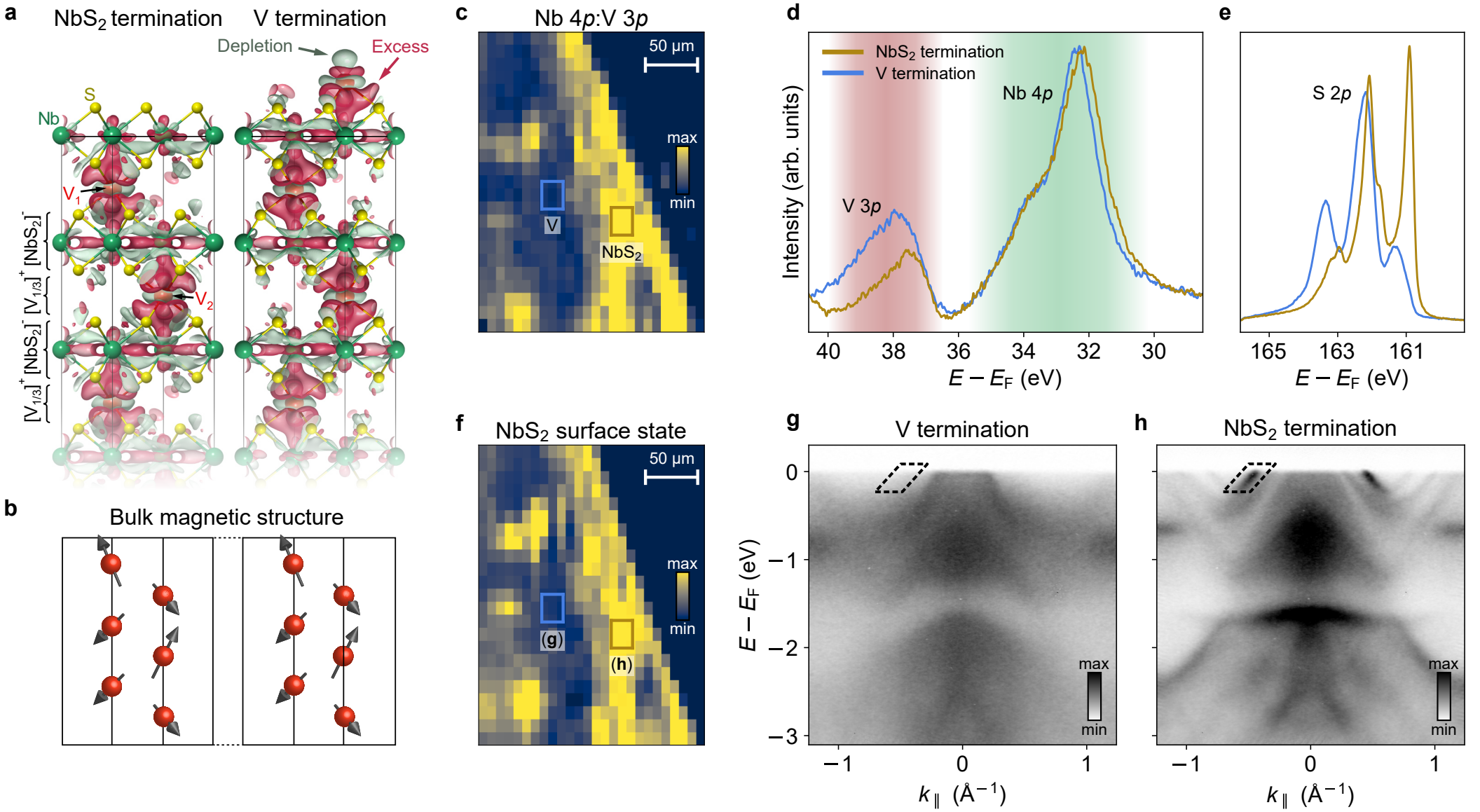
a
NbS2 termination
V termination
Depletion
Excess
S
Nb
V1
V2
[V1/3]+ [NbS2]- [V1/3]+ [NbS2]-
b
Bulk magnetic structure
c
Nb 4p:V 3p
50 μm
max
min
V
NbS2
d
NbS2 termination
V termination
Nb 4p
V 3p
Intensity (arb. units)
40 38 36 34 32 30
E − EF (eV)
e
S 2p
165 163 161
E − EF (eV)
f
NbS2 surface state
50 μm
max
min
(g)
(h)
g
V termination
E − EF (eV)
0 −1 −2 −3
−1 0 1
k∥ (Å−1)
max
min
h
NbS2 termination
−1 0 1
k∥ (Å−1)
max
min

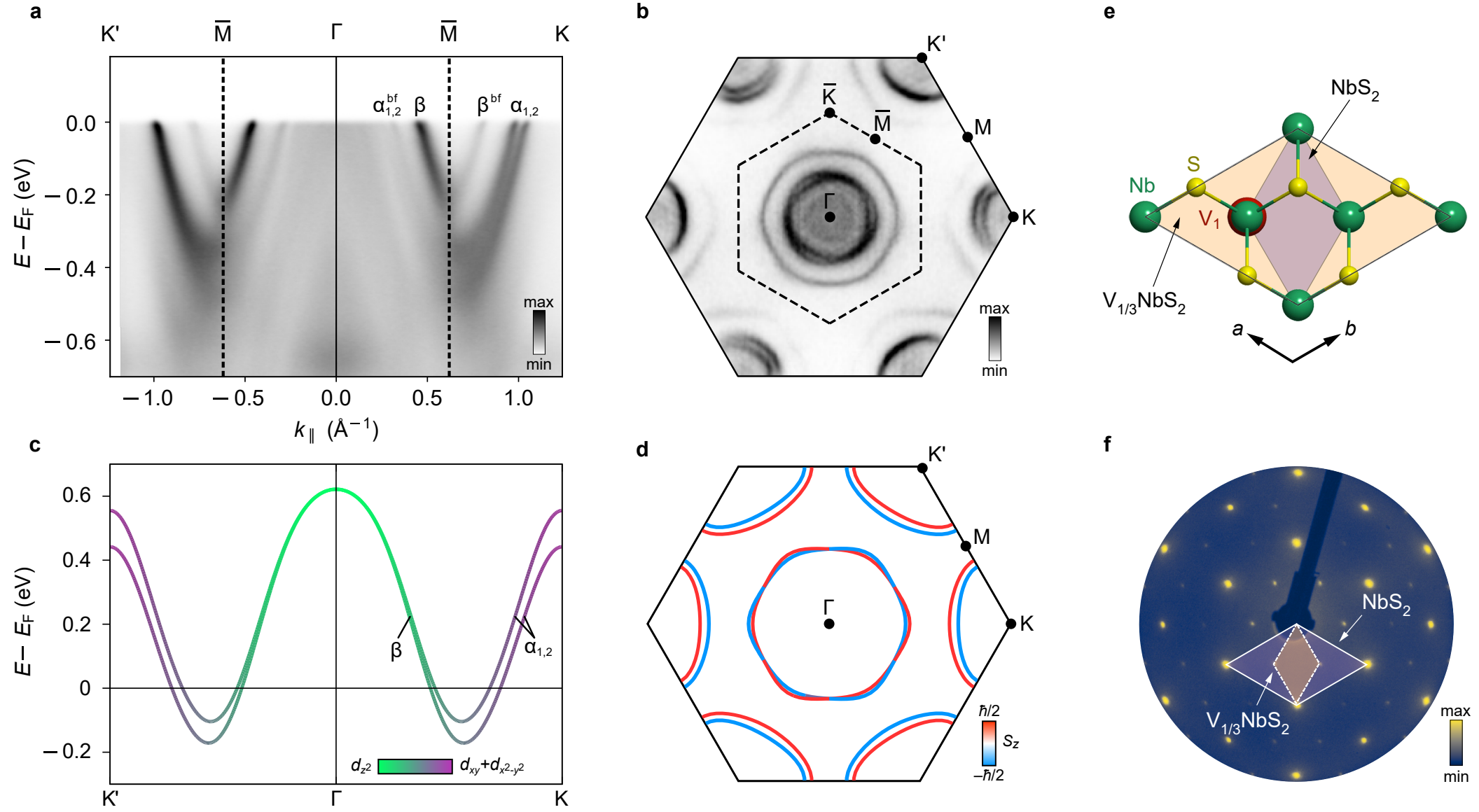
a
K'
M̄
Γ
M̄
K
α^bf_1,2
β
β^bf
α1,2
0.0
−0.2
−0.4
−0.6
E − EF (eV)
max
min
−1.0
−0.5
0.0
0.5
1.0
k∥ (Å−1)
b
K'
K̄
M̄
M
K
Γ
max
min
e
NbS2
S
Nb
V1
V1/3NbS2
a
b
c
0.6
0.4
0.2
0
−0.2
E − EF (eV)
β
α1,2
dz2
dxy+dx2−y2
K'
Γ
K
d
K'
M
Γ
K
ħ/2
Sz
−ħ/2
f
NbS2
V1/3NbS2
max
min

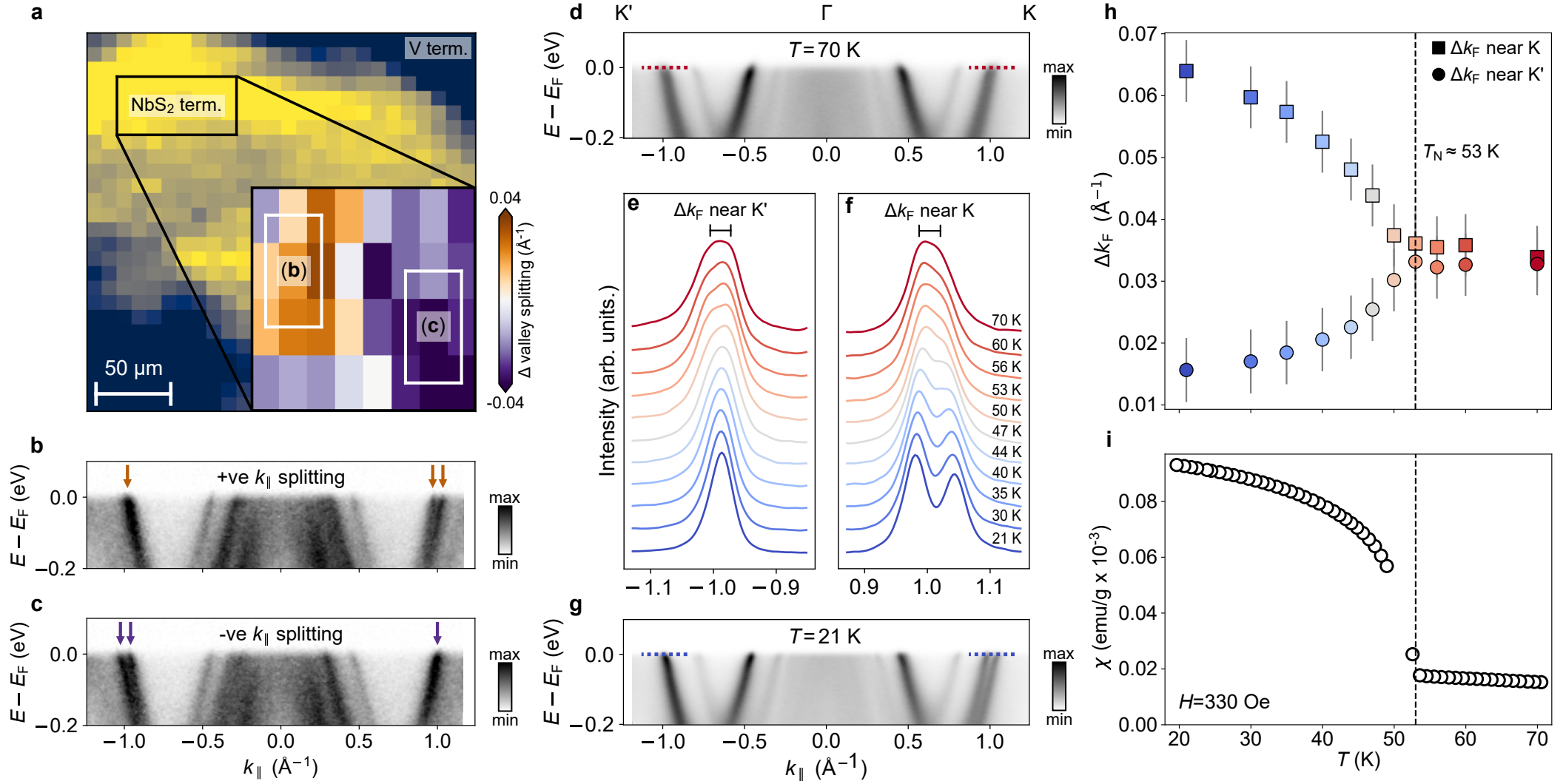
a
V term.
NbS2 term.
(b)
(c)
50 μm
0.04
-0.04
Δ valley splitting (Å⁻¹)
b
+ve k∥ splitting
E − EF (eV)
0.0
−0.2
max
min
c
-ve k∥ splitting
−1.0
−0.5
0.0
0.5
1.0
k∥ (Å⁻¹)
d
K'
Γ
K
T = 70 K
e
Δk_F near K'
f
Δk_F near K
Intensity (arb. units.)
70 K
60 K
56 K
53 K
50 K
47 K
44 K
40 K
35 K
30 K
21 K
−1.1
−1.0
−0.9
0.9
1.0
1.1
g
T = 21 K
h
Δk_F near K
Δk_F near K'
T_N ≈ 53 K
Δk_F (Å⁻¹)
0.07
0.06
0.05
0.04
0.03
0.02
0.01
i
χ (emu/g x 10⁻³)
0.08
0.06
0.04
0.02
0.00
H=330 Oe
20
30
40
50
60
70
T (K)

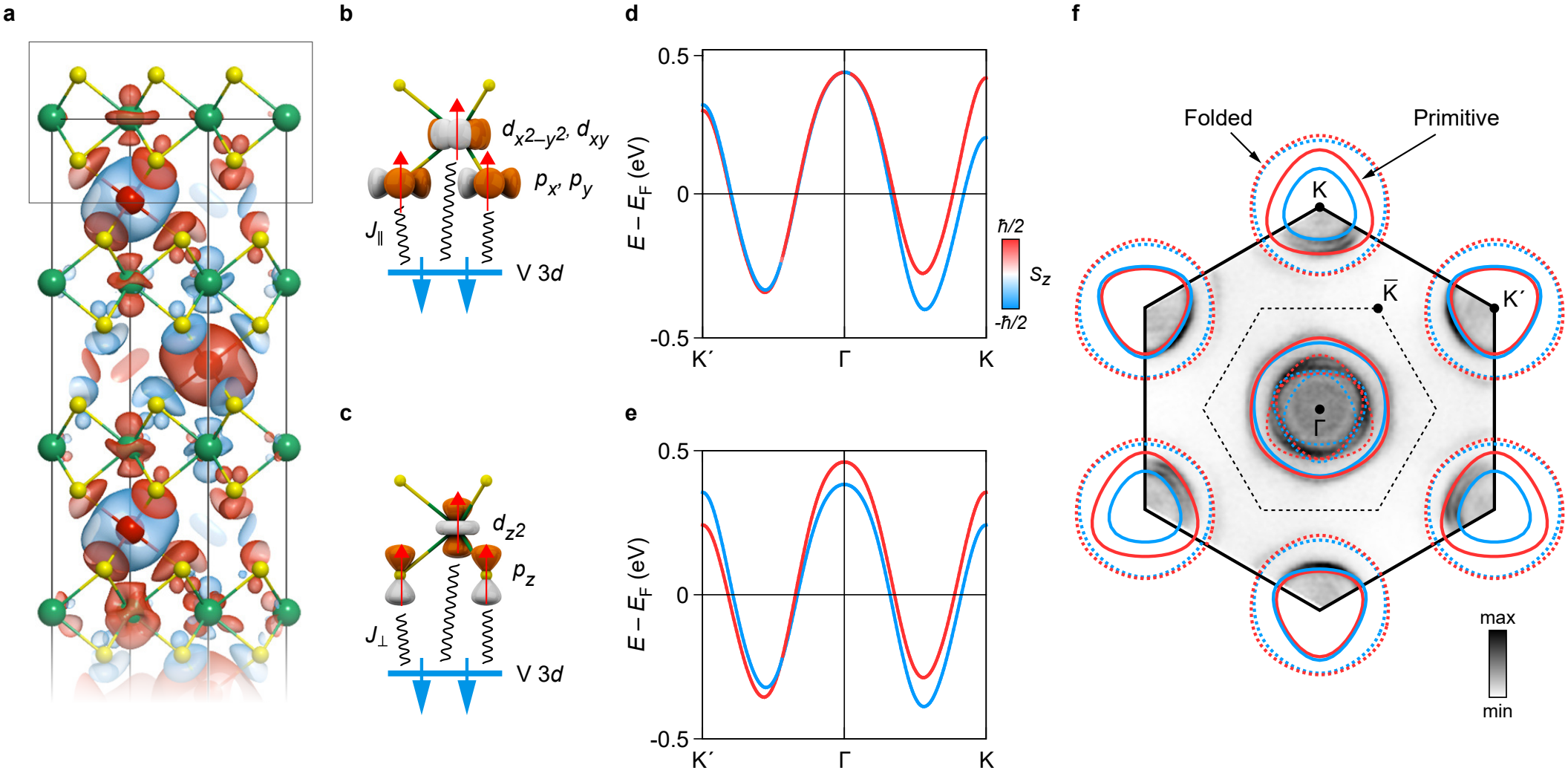
a
b
d_{x2-y2}, d_{xy}
p_x, p_y
$J_{\parallel}$
V 3d
c
d_{z2}
p_z
$J_{\perp}$
V 3d
d
0.5
0
-0.5
$E - E_F$ (eV)
K´
Γ
K
ħ/2
S_z
-ħ/2
e
0.5
0
-0.5
$E - E_F$ (eV)
K´
Γ
K
f
Folded
Primitive
K
$\bar{K}$
K´
Γ
max
min